









Computational Study on Co-Combustion of Coal and Blast Furnace Gas in an Industrial Fluidized Bed Boiler

Swaroop Jena¹, Vasujeet Singh¹, Pruthiviraj Nimalipuri^{1*}, Harish Chandra Das¹, Malay Kumar Pradhan², Vivek Vitankar³

¹ Department of Mechanical Engineering, National Institute of Technology Meghalaya, Shillong 793003, India

² Factories & Boilers, Bhubaneswar 751001, India

³ FluiDimensions, Pune 411045, India

Corresponding Author Email: pruthivirajnimalipuri@gmail.com

Copyright: ©2026 The authors. This article is published by IETA and is licensed under the CC BY 4.0 license (<http://creativecommons.org/licenses/by/4.0/>).

<https://doi.org/10.18280/ijht.440224>

ABSTRACT

Received: 1 February 2026

Revised: 12 April 2026

Accepted: 21 April 2026

Available online: 30 April 2026

Keywords:

circulating fluidized bed combustion, Eulerian-Eulerian, Blast Furnace Gas, coal, multiphase flow modelling

The declining availability of coal has encouraged the investigation of co-firing strategies that combine coal with industrial byproduct gases as a viable alternative energy approach. Conducting experiments on full-scale circulating fluidized bed combustion (CFBC) boilers is both expensive and time-consuming, making numerical simulation an attractive option due to its lower cost and enhanced control over process variables. In this study, an industrial CFBC boiler is numerically modelled to examine the combustion of coal and coal-gas blends, specifically a mixture of 90% coal and 10% Blast Furnace Gas (BFG). The simulation employs a Eulerian-Eulerian multiphase framework to represent three interacting phases: coal particles, bed material (sand), and the gas mixture. Particle interactions, including collision dynamics and contact forces within the granular medium, are described using the kinetic theory of granular flows (KTGF). The reliability of the computational model is verified through comparison with real-time plant measurements such as temperature distribution, pressure drop, bed height, suspension density, and void fraction. A detailed assessment is performed for both pure coal firing and blended fuel operation, with emphasis on axial velocity profiles, temperature behaviour of solid and gaseous phases, gas composition, and pollutant formation, including SO₂ and NO. The results reveal the internal circulation patterns of solid particles within the fluidized bed and demonstrate that blending 10% BFG with coal improves combustion performance. Compared with pure coal combustion, the blended fuel case produces an 8.12% reduction in pressure drop and decreases CO, SO₂, and NO mass fractions by 4.11%, 11.15%, and 6.13%, respectively.

1. INTRODUCTION

Fossil fuels, which are formed over millions of years from organic matter, continue to dominate global energy consumption. However, rapid industrialization and the growing demand for energy have accelerated the depletion of these resources. This situation has created an urgent need for efficient fuel utilization strategies and the development of alternative energy approaches. Among these approaches, fuel co-combustion has emerged as an effective technique for improving fuel flexibility while reducing dependence on conventional fossil fuels. Biomass-based granular solid fuels, such as sawdust, wood chips, and recycled wood waste, are increasingly being utilized for thermal energy production due to their high energy density and wide availability. However, their combustion can lead to environmental concerns, including air pollution and greenhouse gas emissions [1, 2].

Blast Furnace Gas (BFG), a low-calorific-value byproduct generated during the ironmaking process, mainly consists of CO, CO₂, and N₂, with smaller fractions of H₂ and CH₄. The efficient utilization of BFG, particularly through co-

combustion with coal, has attracted significant attention due to its potential to improve overall energy efficiency in industrial applications. Previous investigations have demonstrated the feasibility of using BFG in reheating furnaces with advanced burner configurations, enabling the achievement of high operating temperatures without the need for supplementary fuels [3]. Additionally, combustion characteristics and flame stability of BFG-based fuel mixtures have been investigated under industrial conditions, highlighting the influence of hydrogen content and operational parameters on combustion dynamics [4].

Fluidized bed combustion (FBC) is widely recognized as a suitable technology for co-combustion due to its excellent mixing, fuel adaptability, and lower emissions. Experimental studies have provided insights into particle dynamics, circulation behavior, and energy efficiency in fluidized beds [5-8]. However, such experiments are often expensive, time-consuming, and limited in capturing detailed flow and reaction phenomena [9, 10].

To overcome these limitations, Computational Fluid Dynamics (CFD) has emerged as a powerful tool for analyzing

multiphase reacting systems. Both Eulerian–Lagrangian and Eulerian–Eulerian approaches have been extensively applied in fluidized bed simulations [11–15]. Comparative studies indicate that while the Eulerian–Lagrangian method provides detailed particle-scale resolution, the Eulerian–Eulerian approach offers better computational efficiency and scalability for industrial systems, with comparable accuracy in predicting hydrodynamic behavior [16, 17]. Furthermore, incorporation of the Kinetic Theory of Granular Flow (KTGF) enables accurate representation of solid-phase interactions and bed dynamics [18]. Advanced CFD studies have also successfully modeled complex reacting systems such as fluid catalytic cracking regenerators and chemical looping combustion processes [4, 5].

Despite these advancements, most existing research is limited to single-fuel combustion systems or laboratory-scale configurations. Comprehensive studies addressing the co-combustion of coal and BFG in industrial scale circulating fluidized bed (CFB) boilers, particularly with validation against real plant data, remain scarce.

To address this gap, the present study investigates a 67 TPH circulating fluidized bed combustion (CFBC) boiler operating in an integrated steel plant. A three-dimensional CFD model based on the Eulerian–Eulerian approach is developed and validated using industrial measurements, including pressure, temperature, and phase distribution along the boiler height. Following validation, the model is applied to analyze the co-combustion of coal and BFG, focusing on temperature distribution, species evolution, emission characteristics, and the interaction of homogeneous and heterogeneous reactions.

The outcomes of this study provide both scientific and practical significance by offering a validated computational framework for industrial-scale co-combustion systems. The proposed approach can support design optimization, improve fuel utilization, and reduce dependence on costly experimental investigations, thereby contributing to more sustainable energy practices in the steel and power sectors.

2. NOVELTY AND RESEARCH GAP

Although extensive mathematical models exist for lab-scale CFB combustors, studies addressing combustion involving a coal and BFG mixture are sparse in CFBC. There is a lack of comprehensive studies addressing co-combustion of coal and BFG in industrial-scale CFBC boilers, detailed multiphase CFD modeling using the Eulerian–Eulerian approach, and validation with real plant operating data (temperature, pressure, and phase distribution). The Eulerian–Eulerian (E-E) method provides an advanced understanding of fluidized bed dynamics, heat transfer, and mass transfer.

Focuses on a real-world application—a 67 TPH CFBC boiler within an integrated steel plant—bridging the gap between lab-scale and industrial-scale studies. Employs the Eulerian–Eulerian multifluid method for detailed 3D computational modeling, capturing intricate interactions within the boiler.

Introduces a CFD model capable of replacing traditional semi-empirical and empirical methods for scaling up CFB boilers, offering: Quantitative and qualitative profiles for key variables, Insights that are challenging to achieve through experimental methods.

3. MATHEMATICAL MODELLING

3.1 Geometry creation

The computational domain of the CFBC boiler includes the distributor plate, coal feed inlets, secondary air-ports, and the riser section as depicted in Figure 1. At the base of the reactor, the distributor plate is equipped with 300 circular nozzles, ensuring uniform air distribution into the riser. Coal is supplied through two feed inlets mounted on the side walls, each having a cross-sectional area of 500 mm × 500 mm. In addition, seven secondary air-ports measuring 200 mm × 200 mm are positioned along the front and rear riser walls to enhance mixing and combustion. The riser geometry is divided into two distinct regions: a lower section that gradually diverges to a height of 4000 mm and an upper straight section extending 15,000 mm. Under bubbling fluidized bed operating conditions, only a small fraction of solid particles reach the cyclone zone. For this reason, the cyclone section is excluded from the numerical model used in the present study.

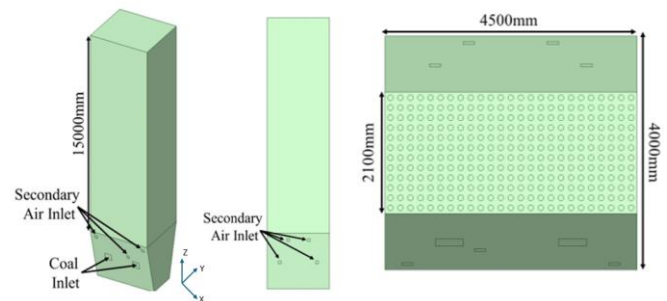


Figure 1. Computational domain

Table 1. Grid independency test

| Mesh Count | Pressure Drop (kPa) |
|------------|---------------------|
| 482,642 | 6.23 |
| 792,365 | 7.25 |
| 1,046,862 | 8.42 |
| 1,457,482 | 8.43 |
| 1,757,832 | 8.43 |



Figure 2. Meshing

3.2 Discretization

The domain is divided into a total of 1,457,482 hexahedral

cells, a count established through a rigorous grid independence test performed across a range of cell counts (482,642, 792,365, 1,046,862, 1,457,482, and 1,757,832), as shown in Table 1. During this test, results showed convergence and stability once the cell count reached 1,457,482, indicating a sufficient level of accuracy for capturing the flow and combustion characteristics within the CFBC boiler. While 1,457,482 cells were determined to be optimal for computational efficiency without compromising accuracy, additional calculations were performed at 1,457,482 cells. The discretised domain is depicted in Figure 2.

The findings from this denser grid are detailed in the results and discussion section to provide a thorough validation and ensure the robustness of the model outcomes.

3.3 Governing equation

Mass balance equations for the gas and solid phases:

$$\frac{\partial(\alpha_g \rho_g)}{\partial t} + \nabla(\alpha_g \rho_g v_g) = 0 \quad (1)$$

$$\frac{\partial(\alpha_c \rho_c)}{\partial t} + \nabla(\alpha_c \rho_c v_c) = 0 \quad (2)$$

$$\frac{\partial(\alpha_s \rho_s)}{\partial t} + \nabla(\alpha_s \rho_s v_s) = 0 \quad (3)$$

Momentum balance equations for the gas and particle phases:

$$\begin{aligned} & \frac{\partial(\alpha_g \rho_g v_g)}{\partial t} + \nabla(\alpha_g \rho_g v_g v_g) \\ & = -\alpha_g \nabla P + \nabla \tau_g + \alpha_g \rho_g \vec{g} + F_{ext} \end{aligned} \quad (4)$$

$$\begin{aligned} & \frac{\partial(\alpha_c \rho_c v_c)}{\partial t} + \nabla(\alpha_c \rho_c v_c v_c) \\ & = -\alpha_c \nabla P - \nabla P_c + \nabla \tau_c + \alpha_c \rho_c \vec{g} - F_{ext} \end{aligned} \quad (5)$$

$$\begin{aligned} & \frac{\partial(\alpha_s \rho_s v_s)}{\partial t} + \nabla(\alpha_s \rho_s v_s v_s) \\ & = -\alpha_s \nabla P - \nabla P_s + \nabla \tau_s + \alpha_s \rho_s \vec{g} - F_{ext} \end{aligned} \quad (6)$$

In the Eulerian-Eulerian granular model P_c and P_s is calculated as follows [19]:

$$P_c = \alpha_c \rho_c \theta_c + 2\rho_c(1 + e_{cc})\alpha_c^2 g_o \theta_c \quad (7)$$

$$P_s = \alpha_s \rho_s \theta_s + 2\rho_s(1 + e_{ss})\alpha_s^2 g_o \theta_s \quad (8)$$

$$g_o = [1 - (\frac{\alpha_s}{\alpha_{s_{max}}})^{1/3}]^{-1} \quad (9)$$

and, τ_g , τ_c and τ_s are the stress tensor for the gas, coal, and sand phases.

$$\tau_g = \alpha_g \mu_g (\nabla v_g + \nabla v_g^t) - \frac{2}{3} \alpha_g \mu_g (\nabla \cdot v_g) \bar{I}_g \quad (10)$$

$$\tau_c = \alpha_c \mu_c (\nabla v_c + \nabla v_c^t) - \alpha_c \left(\varepsilon_c - \frac{2}{3} \mu_c \right) \cdot \vec{v}_c \quad (11)$$

$$\tau_s = \alpha_s \mu_s (\nabla v_s + \nabla v_s^t) - \alpha_s \left(\varepsilon_s - \frac{2}{3} \mu_s \right) \cdot \vec{v}_s \quad (12)$$

Mathematical formulae for granular temperature and solid viscosity, particularly for the coal phase, are shown in the next section. We will also apply an analogous set of equations to the sand phase:

$$\mu_c = \mu_{collisional} + \mu_{kin} + \mu_{friction}$$

Ding and Gidaspow [20] and Lun [21] provide the formulae for shear, kinetic, and collisional viscosities, which are given in terms of particle diameter and the restitution coefficient.

3.3.1 Collisional viscosity

$$\mu_{col} = \frac{4}{5} \alpha_c \rho_c d_c g_o (1 + e_{cc}) \left(\frac{\theta_c}{\pi} \right)^{1/2} \quad (13)$$

Viscosity due to fluctuation in kinetic energy:

$$\mu_{kin} = \frac{\alpha_c d_c \rho_c \sqrt{\theta_c \pi}}{6(3 - e_{cc})} \left[1 + \frac{2}{5} (1 + e_{cc}) (3e_{cc} - 1) \alpha_c g_o \right] \quad (14)$$

3.3.2 Frictional viscosity

$$\mu_f = \frac{P_c \sin \phi}{2\sqrt{I_{2D}}} \quad (15)$$

The mixture technique is used to describe turbulence interactions between the solid and gas phases. By examining the mixture's combined characteristics and velocities, this model illustrates important aspects of turbulent flow. Below is the model's governing equation for the turbulent mixture.

$$\begin{aligned} & \frac{\partial}{\partial t} (\rho_m k) + \nabla \cdot (\rho_m v_m k) \\ & = \nabla \cdot \left(\frac{\mu_{t,m}}{\sigma_k} \nabla k \right) + G_{k,m} - \rho_m \varepsilon \end{aligned} \quad (16)$$

$$\begin{aligned} & \frac{\partial}{\partial t} (\rho_m \varepsilon) + \nabla \cdot (\rho_m v_m \varepsilon) \\ & = \nabla \cdot \left(\frac{\mu_{t,m}}{\sigma_\varepsilon} \nabla \varepsilon \right) + \frac{\varepsilon}{k} (C_{1e} G_{k,m} - C_{2e} \rho_m \varepsilon) \end{aligned} \quad (17)$$

$$\rho_m = \sum_{i=1}^N \alpha_i \rho_i \quad (18)$$

$$\vec{v}_m = \frac{\sum_{i=1}^N \alpha_i \rho_i v_i}{\sum_{i=1}^N \alpha_i \rho_i} \quad (19)$$

where, $\mu_{t,m}$ is turbulent viscosity, calculated as:

$$\mu_{t,m} = \rho_m C_\mu \frac{k^2}{\varepsilon} \quad (20)$$

where, $C_\mu = 0.09$ and $G_{k,m}$ is turbulent kinetic energy production given below:

$$G_{k,m} = \mu_{t,m} (\nabla v_m + (\nabla v_m)^T) : \nabla v_m \quad (21)$$

KTGF is applied to represent the fluctuating motion of particles and their associated kinetic energy. Due to the random movement of particles, their fluctuating energy

component is expressed through a parameter commonly referred to as the granular temperature [22, 23]. The governing transport equation derived from kinetic theory is presented below:

$$\begin{aligned} & \frac{3}{2} \left[\frac{\partial}{\partial t} (\alpha_c \rho_c \theta_c) + \nabla \cdot (\alpha_c \rho_c v_c \theta_c) \right] \\ & = (-P_c \bar{I} + \tau_c) \cdot \nabla v_c - \gamma_{\theta_c} + \nabla \cdot (k_{\theta_c} \nabla \theta_c) + 3K_{gc} \theta_c \end{aligned} \quad (22)$$

Within this formulation, the first term on the right-hand side represents energy production caused by the solid stress tensor. The second term corresponds to energy diffusion, while the third accounts for collisional dissipation. The final contribution describes interphase energy exchange. Each term in the equation is expressed as a function of granular temperature, solids pressure, solids viscosity, and bulk viscosity. The coefficient k_{θ_c} denotes the diffusive constant for the coal phase and is defined in Eq. (20):

$$\begin{aligned} k_{\theta_c} = & \frac{150 \rho_c d_c \sqrt{\theta_c \pi}}{384(1 + e_{cc})g_o} \left[1 + \frac{6}{5} \alpha_c g_o (1 + e_{cc}) \right]^2 \\ & + 2\alpha_c^2 \rho_c d_c (1 + e_{cc}) g_o \sqrt{\frac{\theta_c}{\pi}} \end{aligned} \quad (23)$$

$$\gamma_{\theta_c} = \frac{12(1 - e_{cc})^2 g_o}{d_c \sqrt{\pi}} \alpha_c^2 \rho_c \theta_c^{3/2} \quad (24)$$

For highly dense FB, the convection and diffusion variables may be disregarded since the algebraic equation, which is the second version of the granular temperature equation, shows that the granular energy generation and dissipation rates are in equilibrium [24].

$$0 = (-P_c \bar{I} + \tau_c) \cdot \nabla v_c - \gamma_{\theta_c} + 3K_{gc} \theta_c \quad (25)$$

3.3.3 Interfacial force characterization

Interactions between gas and solid phases involve several interfacial forces, including drag, lift, and virtual mass effects. Among these, the drag force between coal particles and the gas phase is the primary focus of this section. The sand phase is modeled using an equivalent set of governing relations.

$$\begin{aligned} F_{ext} &= F_{drag} + F_{lift} + F_{vm} \\ F_{drag} &= K_{cg} (v_g - v_c) \end{aligned}$$

Numerous empirical and semi-empirical expressions for the drag coefficient have been reported in the literature for gas–solid fluidized systems. The correlations most frequently applied include the Gidaspow model [25], the Wen and Yu formulation [26], and the Syamlal–O’Brien model (1988). The predicted distributions of gas and solids volume fractions, as well as overall flow structures, are strongly dependent on the selected drag closure. For bubbling fluidized beds, the Syamlal–O’Brien correlation is widely recognized as one of the most reliable options and is therefore adopted in the present work. The corresponding expression for the drag interaction is given below:

$$K_{cg} = \frac{3\alpha_c \alpha_g \rho_g}{4v_{rc}^2 d_c} C_d \left(\frac{Re_c}{v_{rc}} \right) (v_g - v_c) \quad (26)$$

The interphase momentum exchange coefficient is adjusted using a terminal settling velocity relationship, where v_{rc} represents the ratio of a particle’s terminal settling velocity to that of an equivalent spherical particle.

$$\begin{aligned} v_{rc} &= 0.5 \left(A - 0.06 Re_c \right. \\ & \left. + \sqrt{(0.06 Re_c)^2 + 0.12 Re_c (2B - A) + A^2} \right) \end{aligned} \quad (27)$$

$$\begin{aligned} A &= \alpha_g^{4.14} \\ B &= 0.8 \alpha_g^{1.28} \text{ For } \alpha_g < 0.85 \\ B &= \alpha_g^{2.65} \text{ For } \alpha_g > 0.85 \end{aligned}$$

$$C_d = \left(0.63 + \frac{4.8}{\sqrt{\frac{Re_s}{v_{rc}}}} \right) \quad (28)$$

$$Re_c = \frac{\rho_g (v_g - v_c) d_c}{\mu_g}$$

3.3.4 Formulation for species mass fraction transport

A finite-rate/eddy-dissipation formulation is adopted to describe the kinetics of homogeneous reactions. In this approach, the overall reaction rate is determined by selecting the smaller value predicted by either the chemical finite-rate expression or the turbulence-controlled eddy dissipation mechanism [27, 28].

$$\hat{R}_{i,r} = \Gamma (v''_{i,r} - v'_{i,r}) \left(k_{fr} \prod_{j=1}^N [C_{j,r}]^{(n'_{i,r} + n''_{i,r})} \right) \quad (29)$$

The stoichiometric coefficients of reactants and products are represented by v'_{ij} and v''_{ij} , respectively. Here, k_{fr} denotes the forward reaction rate constant, and C_j corresponds to the molar concentration of species j . The parameter N indicates the total number of chemical species involved in the reaction system. The subsequent relation defines the reaction rate contribution associated with turbulent eddy dissipation.

$$\hat{R}_{i,r} = v'_{i,r} M_{w,i} A B \rho \frac{\varepsilon}{k} \frac{\sum_p Y_p}{\sum_j^n v_{j,r}^n M_{w,i}} \quad (30)$$

The turbulence-generated kinetic energy is represented by k , while its dissipation rate is indicated by ε . Unless otherwise specified, the empirical model constants take default values of $A = 4$ and $B = 0.5$. The molecular weight and mass fraction of the i^{th} chemical species are expressed as $M_{w,i}$ and Y_i , respectively.

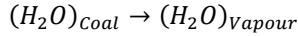
3.4 Rate equation for solid gas reaction system

Coal is composed primarily of ash, moisture, fixed carbon, and volatile matter. In contrast, BFG is a gaseous fuel mixture containing roughly 25% CO, 20% CO₂, 3% H₂, and 52% N₂ [6]. When introduced into the boiler, coal and BFG undergo a sequence of both heterogeneous and homogeneous reactions with the surrounding gas environment. Because these fuels differ substantially in their physical characteristics and chemical behavior, separate kinetic parameters are required to

accurately represent their combustion processes.

The literature has plenty of information on the kinetic parameters and reaction rates for coal's heterogeneous processes, including char oxidation, tar oxidation, moisture evaporation, volatile release, and char interactions with CO₂, H₂O, and NO [29, 30]. In this study, relevant kinetic parameters from various sources have been used to model these coal reactions. C programming is used for creating the intrinsic reaction rates for the heterogeneous processes, which are then integrated into the Fluent solver via a user-defined function (UDF). Below provides a summary of the kinetics and stoichiometry of the heterogeneous reactions between various phases.

3.4.1 Coal moisture release

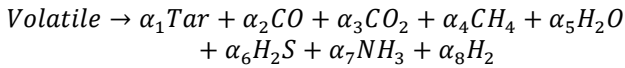


$$R_{mr} = A_{drying} \times \exp\left(-\frac{E_{drying}}{R_{gas} \cdot T_c}\right) \alpha_c \rho_c Y_{(H_2O)_{coal}} \quad (R1)$$

Here, R_{gas} represents the universal gas constant, and T_c denotes the coal particle temperature. The term $Y_{H_2O,coal}$ corresponds to the moisture mass fraction within the coal. The parameters A_{drying} and E_{drying} are the pre-exponential factor and activation energy associated with the drying process of the coal phase.

3.4.2 Coal devolatilization

During coal devolatilization, various gaseous hydrocarbons are released, including CH₄, H₂O (vapor), CO₂, CO, H₂S, NH₃, and tar. The MGAS model [31] serves as the basis for the devolatilization rate in this investigation. Mass balance calculations are used to calculate the stoichiometric coefficients for the devolatilization reaction as well as the molecular formulae for tar and volatile matter.



$$R_d = \begin{cases} A_{coal_devolatilization} \times \exp\left(-\frac{E_{coal_devolatilization}}{R_{gas} \cdot T_c}\right) (1-\alpha_c) \rho_c (Y_{VM,coal} - Y^*) & Y_{VM,coal} \geq Y^* \\ 0 & Y_{VM,coal} < Y^* \end{cases} \quad (R2)$$

$$Y^* = \frac{\rho_{c_o} (Y_{FC_o} + Y_{VM_o}) Y_o^*}{\rho_c}$$

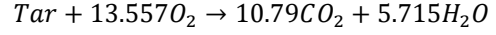
$$Y_o^* = \begin{cases} \left(\frac{867.2}{(T_c - 273)/100}\right)^{3.914} & T_c < 1223 \\ 0 & T_c \geq 1223 \end{cases}$$

Here, Y_{VM} represents the instantaneous mass fraction of volatile matter remaining in the coal. The parameters $Y_{FC,0}$ and $Y_{VM,0}$ denote the initial mass fractions of fixed carbon and volatile matter, respectively. The quantity Y^* defines the remaining fraction of volatile material in the solid phase.

3.4.3 Tar oxidation

When coal devolatilizes, tar—a viscous, black, and sticky

liquid—is created. It is made up of intricate chemical molecules that include a lot of carbon. Tar oxidizes when it meets oxygen, producing CO₂ and H₂O. The tar oxidation kinetics and stoichiometry used in this investigation are taken from the study [29].

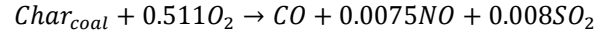


$$R_{tar_oxidation} = A_{tar_oxidation} \times \exp\left(-\frac{E_{tar_oxidation}}{R_{gas} \cdot T_c}\right) \times \alpha_g \times \left(\frac{\rho_g Y_{O_2}}{M_{W,O_2}}\right)^{1.5} \times \left(\frac{\rho_g Y_{tar}}{M_{W,O_2}}\right)^{0.25} \quad (R3)$$

3.4.4 Char oxidation

Char refers to the solid residue remaining in the furnace after the devolatilization stage of coal conversion. It is primarily composed of carbon, along with smaller quantities of hydrogen, nitrogen, oxygen, and sulphur. Although the detailed mechanisms governing char oxidation are complex and involve multiple interacting processes, the present study adopts a simplified modelling framework [32]. In this representation, char is treated mainly as a carbon-rich solid, while other species released to the gas phase during devolatilization, including hydrogen, nitrogen, and oxygen, are accounted for separately.

Char oxidation is controlled by three dominant resistances: intrinsic surface reaction kinetics, diffusion through the surrounding gas film, and diffusion within the ash layer. The oxidation model proposed in the study [30] is implemented in the current work.



$$R_{char_oxidation} = \frac{6\alpha_c p_{O_2}}{d_c \left(\frac{1}{k_{film}} + \frac{1}{k_{ash}} + \frac{1}{k_r}\right)} \times M_{W,O_2} \quad (R4)$$

$$k_{film} = \frac{D_{O_2} Sh}{d_c \times \frac{R}{M_{W,O_2}} \times T_g}$$

$$D_{O_2} = 4.26 \left(\frac{T_g}{1800}\right)^{1.75}$$

$$Sh = (7 - 10\alpha_g + 5\alpha_g^2) \times (1 + 0.7 Re_c^{0.2} S c^{1/3}) + (1.33 - 2.4\alpha_g + 1.2\alpha_g^2) \times Re_c^{0.2} S c^{1/3}$$

$$k_{ash} = \frac{2r_d D_e}{(1 - r_d) d_c \times \frac{R}{M_{W,O_2}} \times T_c}$$

The current and original carbon mass fractions in the coal particle are used to determine r_d , defined as the ratio between the shrinking char core diameter and the overall particle diameter. The ash layer's effective diffusivity, denoted by D_e , is expressed as follows:

$$D_e = D_{O_2} \left(0.25 + 0.75(1 - Y_{A_o})\right)^{2.5}$$

Table 2. Homogeneous reactions kinetics

| Reaction | A | E(J/k-mol) | Order of Reaction | Reaction No. |
|--|-----------------------|--------------------|-------------------------------|--------------|
| $CO + 0.5O_2 \rightarrow CO_2$ | 1.3×10^{11} | 1.50×10^4 | $[CO][O_2]^{0.5}[H_2O]^{0.5}$ | R7 |
| $CH_4 + 1.5O_2 \rightarrow CO + 2H_2O$ | 5.01×10^{11} | 2.42×10^4 | $[CH_4][O_2]$ | R8 |
| $H_2 + 0.5O_2 \rightarrow H_2O$ | 1.08×10^{13} | 1.52×10^4 | $[H_2]^{1.5}[O_2]^{0.5}$ | R9 |

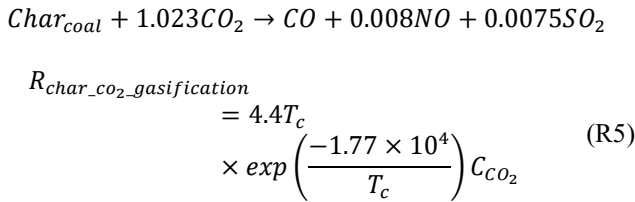
Table 3. Kinetic parameters for the homogeneous gas-phase reactions

| Reaction | A | E(J/kmol) | Order of Reaction | Reaction No. |
|---|-----------------------|--------------------|--------------------------|--------------|
| $H_2S + 1.5O_2 \rightarrow SO_2 + H_2O$ | 2.12×10^{11} | 2.45×10^4 | $[H_2S][O_2]$ | R11 |
| $NH_3 + NO + 0.25O_2 \rightarrow N_2 + 1.5H_2O$ | 3.38×10^{13} | 2.94×10^4 | $[NH_3][NO][O_2]^{0.25}$ | R12 |
| $CO + NO \rightarrow CO_2 + 0.5N_2$ | 1.95×10^7 | 1.9×10^4 | $[CO][NO]$ | R13 |
| $NH_3 + 1.25O_2 \rightarrow NO + 1.5H_2O$ | 2.73×10^{17} | 3.82×10^4 | $[NH_3][O_2]$ | R14 |

$$k_r = 8710 \times \exp\left(\frac{-27000}{R_{gas}T_c}\right) r_d^2$$

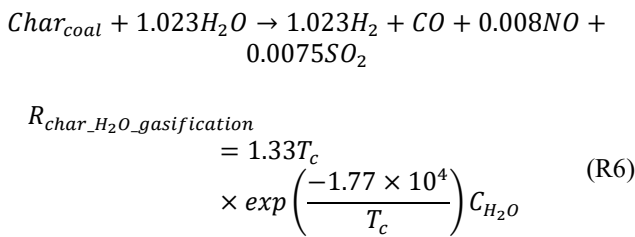
3.4.5 Char reaction with CO₂

By interacting with CO₂, char undergoes gasification, producing CO, NO, and SO₂. The study's char gasification reaction kinetics with CO₂ were taken from the study [33].



3.4.6 Char reaction with H₂O

In addition to oxidation, char reacts with steam to generate gaseous products such as H₂, CO, NO, and SO₂. The gasification behavior of char in the presence of water vapor is modeled using the reaction framework reported in the study [34].



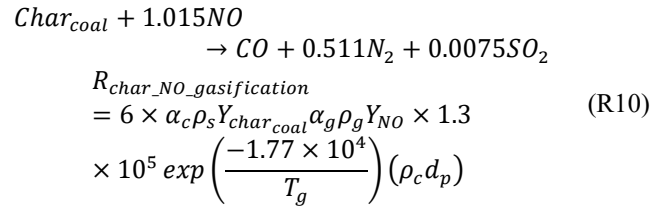
3.4.7 Homogeneous reaction kinetics

Various gas-phase species—such as CO, CH₄, H₂, H₂S, and NH₃—are released through heterogeneous reactions. These species then participate in homogeneous oxidation reactions with O₂. The set of homogeneous reactions incorporated in the present study is listed in Table 2, with rate parameters adopted from the study [34].

3.4.8 Predictive modelling of emission formation

Modelling the development of pollutants is intrinsically difficult, because trace chemical species are involved. The CFD simulation employs a number of simplifications to improve computational performance. During devolatilization, sulphur and nitrogen are released primarily as H₂S and NH₃. These species then react with O₂ through gas-phase homogeneous reactions to form SO₂ and NO, as presented in

Table 3. Additionally, the char residue, which retains some sulphur and nitrogen, further contributes to SO₂ and NO formation during its oxidation. For this study, it is assumed that NO represents the total NO_x emissions. Table 3 lists the pertinent homogeneous reactions that contribute to the creation and degradation of contaminants.



3.5 Boundary conditions

To accurately capture hydrodynamic and combustion behavior, appropriate initial and boundary conditions are established. Preheated primary air enters through bottom nozzles under a uniform mass flow rate, while a coal and BFG mixture is injected from side wall ports. Secondary air is introduced via seven preheated inlets on each side wall. The gas mixture's domain walls are subjected to no-slip conditions, while the solid phases' Specularity coefficient remains constant. The domain exit is defined by a pressure outlet. An initial sand bed occupies the region immediately above the distributor plate, filling the first 700 mm with a solids volume fraction of 0.48. The model considers three Eulerian phases: the gas phase, coal particles acting as fuel, and sand serving as the inert bed material, within an Eulerian–Eulerian multiphase framework. Coal composition is detailed in Table 4, while species involved and mathematical inputs are listed in Tables 5 and 6 respectively. The simulation uses a pressure-based segregated solver with the SIMPLE algorithm for pressure-velocity coupling, second-order upwind discretization, and a transient time step of 0.0001 s with 80 inner iterations for convergence.

Table 4. Characterization of coal via proximate and ultimate techniques

| | Ultimate Analysis | Proximate Analysis | |
|---|-------------------|--------------------|-------|
| C | 43.90% | FC | 32.94 |
| H | 3.60% | VM | 23.40 |
| N | 0.99% | ASH | 28.92 |
| O | 11.65% | M | 14.74 |
| S | 0.55% | LHV (kJ/kg) | 21420 |

Table 5. Identification of Eulerian phases with respective species

| Eulerian Phases | Species |
|-----------------|---|
| Gas Phase | Includes multiple gaseous components such as oxygen, tar, CO, N ₂ , H ₂ S, H ₂ O vapor, CO ₂ , NO, benzene, CH ₄ , SO ₂ , H ₂ , and NH ₃ vapor. |
| Coal Phase | Composed of fixed carbon, ash content, volatile compounds, and inherent moisture. |
| Sand Phase | Contains inert sand particles used as the bed material. |

Table 6. Simulation-specific mathematical inputs

| S. No. | Modelling Parameters | Value |
|--------|---|---|
| 1 | Sand properties | Particle size: 0.28 mm; Density: 2200 kg/m ³ |
| 2 | Coal properties | Particle size: 2 mm; Density: 1400 kg/m ³ |
| 3 | Primary air inlet rate | 12.37 kg/s |
| 4 | Secondary air inlet rate | 12.37 kg/s |
| 5 | Temperature of both primary and secondary air | 554 K |
| 6 | Pure coal combustion – Coal feed rate | 4.17 kg/s |
| 7 | Pure coal combustion – Coal inlet temperature | 300 K |
| 8 | Co-combustion – Coal feed rate | 3.75 kg/s |
| 9 | Co-combustion – BFG feed rate | 0.375 kg/s |
| 10 | Combined fuel inlet temperature (coal + BFG) | 300 K |
| 11 | Restitution coefficient | 0.9 |
| 12 | Specularity Coefficient | 0.1 |
| 13 | Solid phase volume fraction | 0.48 |
| 14 | Initial bed height (static) | 700 mm |
| 15 | Outlet pressure boundary | -50 Pa |

4. RESULTS AND DISCUSSIONS

The previously defined initial and boundary conditions are used to solve the transient governing equations in an iterative

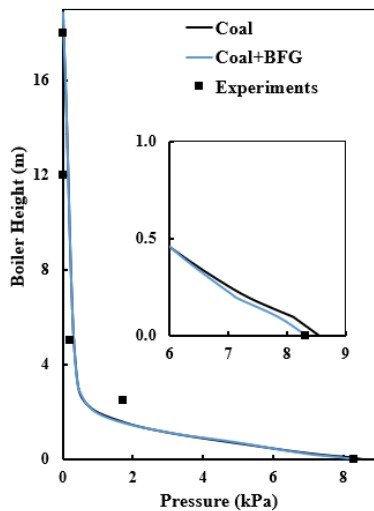


Figure 3. Pressure validation

manner. The total simulated physical time is 60 seconds, with statistical averaging of flow variables performed over the final 40 seconds to ensure stable results. The analysis that follows concentrates on hydrodynamic behavior, heat transfer characteristics, and combustion performance.

4.1 Validation

The accuracy of the numerical model is assessed by comparing simulation outputs with operational measurements obtained from an industrial CFBC boiler installed in an integrated steel plant. Field data were collected during approximately one week of continuous operation at multiple elevations along the boiler height. Instantaneous temperature and pressure readings were monitored at several key locations, including the air distributor, fluidized bed region, screen section, upper furnace, and cyclone inlet. Time-averaged temperature and pressure profiles derived from plant measurements were then compared with CFD predictions, showing strong agreement with the experimental observations. Due to the intense mixing of gas, coal, and sand phases, Figure 3 indicates a larger pressure drop in the lower section of the boiler when real-time measurements are contrasted with simulated pressure distributions along the riser.

The average pressure fluctuation was not significantly affected by the usage of mixed fuel (coal + 10% BFG). Figure 4 further illustrates this trend through pressure contours, indicating that pressure losses are concentrated up to 3 meters, where multiphase mixing occurs, while minimal pressure drop is observed above this height, where only gas is present.

Figure 5 compares the experimental findings with the fluidized bed height predicted by CFD. While CFD tends to slightly overestimate the bed height, it offers a continuous height profile, unlike the point-based experimental method that uses pressure drops at specific locations. For example, a pressure drop of 1.72 kPa at 2.5 m and 0.20 kPa at 5 m led to identifying 2.5 m as the bed height in experiments. Further validation was done by comparing CFD-derived bed voidage and suspension density with values calculated from industrial pressure data using Basu et al.'s model [35]. As illustrated in Figure 6, the CFD results closely match the industrial data, confirming the accuracy and reliability of the CFD approach.

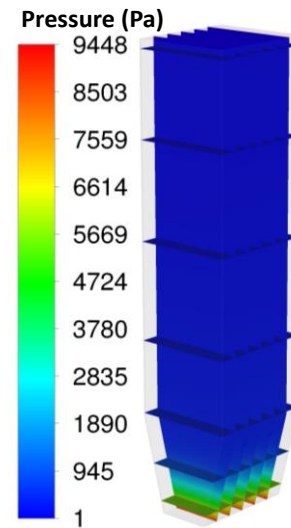


Figure 4. Pressure contour

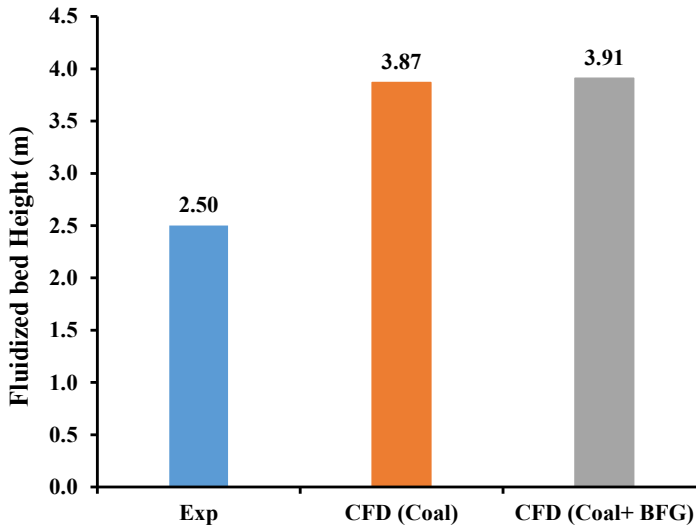


Figure 5. Validation of simulated bed height against plant measurements

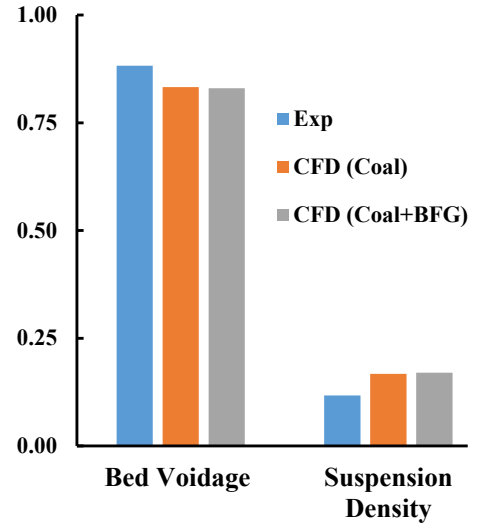


Figure 6. Validation of suspension density and bed voidage

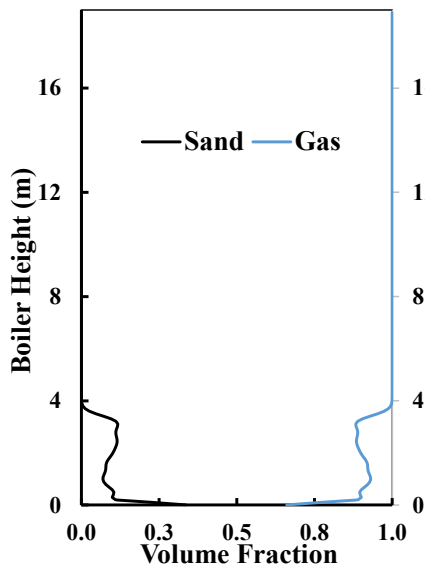


Figure 7. Volume fraction variation along boiler height

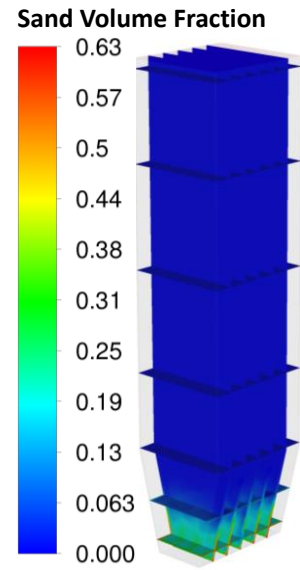


Figure 8. Sand volume fraction contour

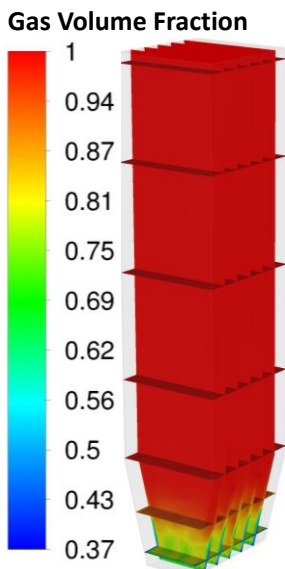


Figure 9. Gas volume fraction contour

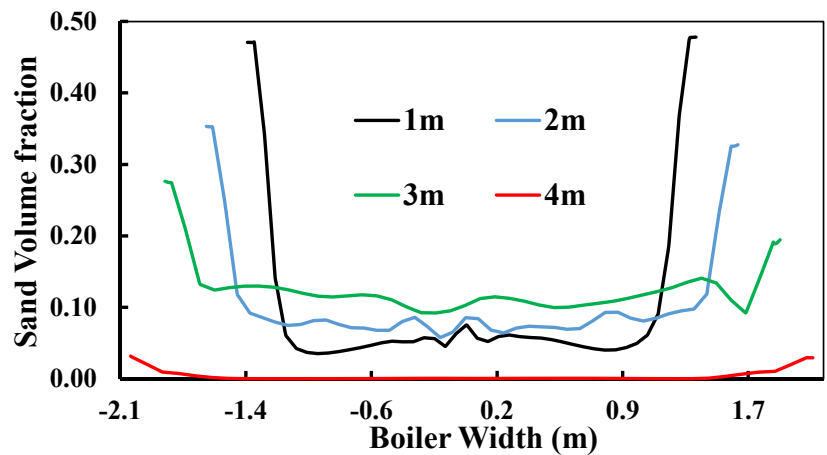


Figure 10. Lateral sand concentration profile

Figure 7 presents the variation of gas and sand volume fractions along the vertical height of the boiler. Strong mixing and bubble dynamics cause the sand concentration to decrease rapidly with elevation, with the highest value (0.41) observed near the bottom of the fluidized bed. The effective bed height can be identified from the sand volume fraction profile: it falls to approximately 0.11 at 1 m above the distributor plate and gradually approaches zero at around 3.91 m. The top border of the fluidized area is confirmed by the almost complete absence of sand particles above this level. Figure 7 also shows the fluctuation of the gas volume fraction, and it is shown that the variation of the gas volume percent is proportional to the variation of the sand volume % along the boiler's height.

The bottom part of the fluidized bed has the lowest gas volume fraction value (0.59). Gas volume fraction increases along the height of the boiler and attains maximum value (1) at 3.91 m height above the distributor plate. Figures 8 and 9 present contour plots of sand and gas volume fractions across different horizontal and vertical sections of the boiler. These contours reveal similar distribution trends for both the gas

mixture and the solid phase. Figure 10 further depicts the variation of sand volume fraction across the boiler width at heights of 1, 2, 3, and 4 meters. Regions near the side walls exhibit a relatively higher concentration of sand. The distribution remains nearly symmetric about the longitudinal centerline of the boiler. Moreover, the results indicate that the sand fraction reaches its peak in the central region at approximately 3 meters above the base and declines to its minimum value near 4 meters.

Vertical lines are depicted in Figure 11, Figures 12 and 13 which show the particle recirculation in the bottom section of the fluidized bed by measuring the axial velocity of the sand along three vertical lines in the boiler. The results show that sand velocity is lowest near the base and increases with height, peaking at 1.65 m/s around 1 meter above the distributor plate. Negative axial velocities near the bottom indicate downward movement. Figures 13 and 14 reveal that near-wall sand flows downward, while central flows move upward, promoting strong recirculation and mixing. This enhances heat and mass transfer, improving coal combustion and overall efficiency.

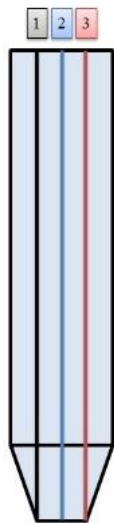


Figure 11. Schematic of boiler

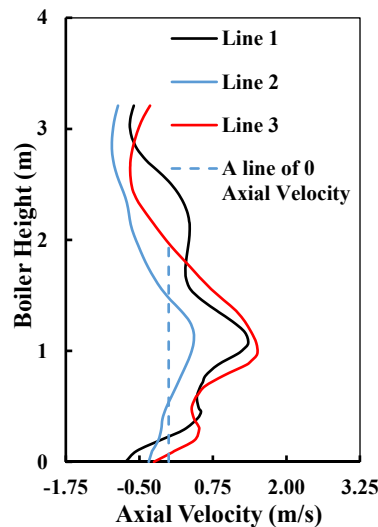


Figure 12. Variation of sand axial velocity

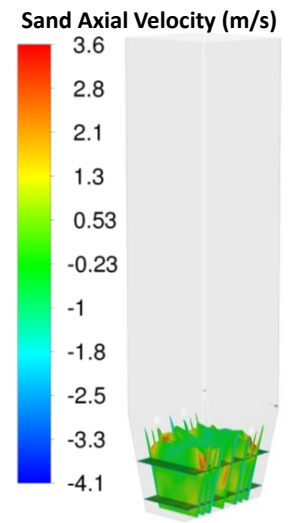


Figure 13. Sand velocity contour

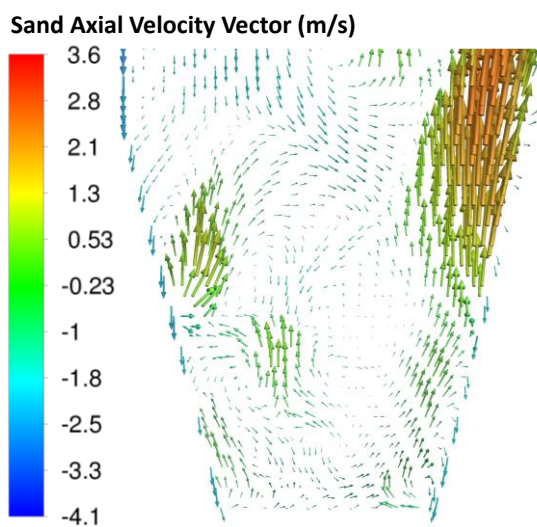


Figure 14. Sand velocity vector

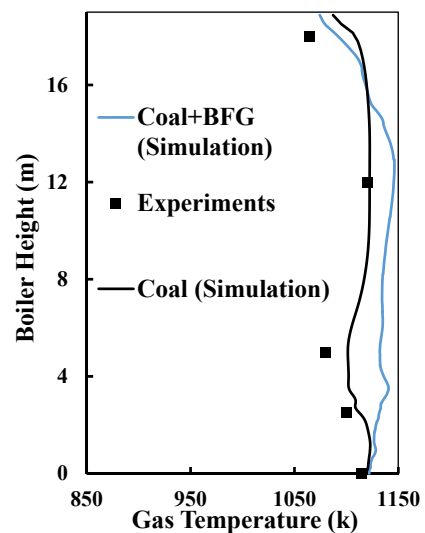


Figure 15. Temperature validation

By contrasting experimental data throughout the boiler height with predicted gas temperatures, the CFD model is further verified. A maximum temperature of 1147.16 K is

observed in the freeboard region, where volatile gases from the coal and 10% BFG mixture combust through exothermic reactions. These gas-phase reactions significantly raise the

temperature in the upper part of the boiler. Compared to pure coal combustion, the blended fuel produces 59.55 K higher temperatures due to faster heat release from homogeneous BFG combustion. The mixing of cooler secondary air (at 554 K) injected between 3 and 6 meters causes the gas temperatures to drop to 1090.41 K (coal) and 1130.62 K (coal + BFG) at 3.88 meters above the distributor plate, as depicted in Figure 15. This cooling effect is evident in Figure 16, where blue and green zones indicate lower temperatures near the air inlets, while warmer tones highlight the freeboard's high-temperature region. Figure 17 illustrates the lateral temperature profiles across the boiler width at multiple elevations, demonstrating strong agreement between CFD predictions and experimental measurements. The results confirm that the simulation successfully captures the thermal behavior of the combustion process. At all examined heights (1 m, 4 m, 7 m, 11 m, 15 m, and 19 m), the temperature distribution remains non-uniform across the width of the boiler. This asymmetry is attributed to the influence of secondary air entering from the side walls, which redirects volatile matter toward the near-wall regions of the fluidized bed. Consequently, temperatures in the central zone are

comparatively lower, while the maximum recorded temperature of 1171.81 K occurs near the wall at approximately 4 m above the base.

Figure 18 presents the variation of sand temperature along the boiler height, with data available up to 3.71 m—the extent of fluidized sand presence. Up to 1 m, sand temperatures remain consistent at 1124.31 K along lines 1 and 3 but slightly decrease to 1117 K above this height due to mixing with cooler secondary air. Lines 1 and 3 show higher temperatures than line 2, as they are positioned closer to the coal inlets, while line 2 is centrally located. Figure 19 displays sand temperature contours, where yellow near secondary air inlets indicates cooling from air mixing, and the uniform orange in the fluidized bed suggests effective mixing and thermal uniformity.

Combustion modelling in the CFBC boiler was conducted after the hydrodynamics and heat transport study, considering both homogeneous and heterogeneous chemical processes. Homogeneous reactions occur within the same phase (e.g., reactions R7 to R9, and R11 to R14), while heterogeneous reactions involve interactions between different phases (e.g., reactions R1 to R6 and R8).

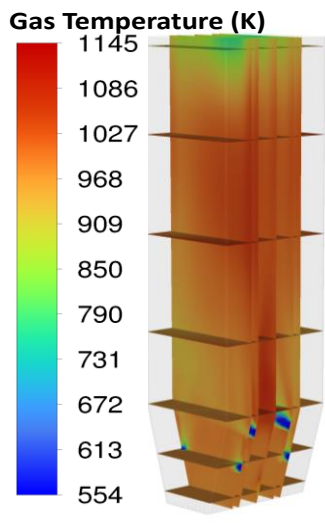


Figure 16. Temperature contour

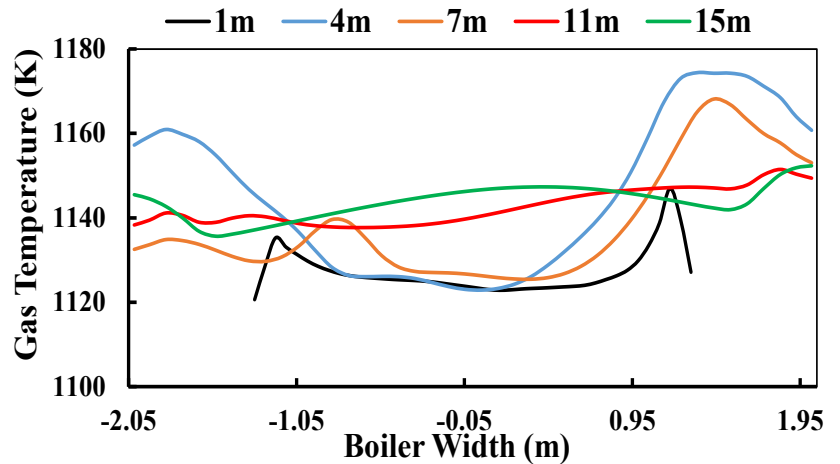


Figure 17. Lateral gas temperature profile

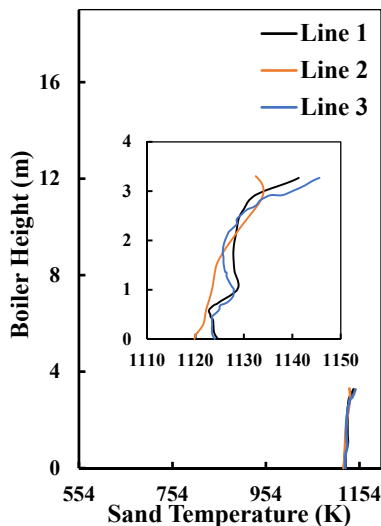


Figure 18. Sand temperature profile along the boiler height

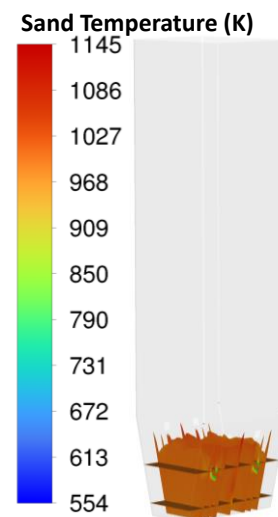


Figure 19. Simulated sand temperature field

The kinetics of the heterogeneous reactions are implemented using a UDF. For efficient combustion of the coal and BFG mixture, a sufficient and well-distributed supply of oxygen is essential. Figure 20 illustrates the O₂ mass fraction profiles along three vertical lines within the boiler during coal and 10% BFG combustion. Line 2 shows the highest O₂ mass fraction (0.21) near the bottom, while lines 1 and 3 exhibit lower values (around 0.09). A general decline in O₂ concentration is observed up to 4 meters in height at all three lines due to the immediate consumption of O₂ by the reactive coal-BFG mixture, forming CO and CO₂. Above 4 meters, O₂ levels rise sharply due to the introduction of secondary air at that height. The contours of the O₂ mass fraction in various horizontal and vertical sections are shown in Figure 21. Bluish zones, which indicate severe oxidation, show a lower O₂ concentration in the boiler's lower central section, particularly above the coal inlets. In contrast, higher O₂ levels appear as orange zones near the front and rear walls and in the upper regions of the boiler, reflecting enhanced oxygen availability due to secondary air entrainment.

Figure 22 illustrates the distribution of O₂ mass fraction across the boiler width at various heights (1 m, 4 m, 7 m, 11 m, 15 m, and 19 m). The O₂ distribution appears symmetrical along the boiler's longitudinal axis. At 1 m height, however, the O₂ mass fraction is uneven across the width, with a peak value of 0.18 at the centre and a lower value of 0.071 near the

walls. This reduction near the walls is attributed to more intense coal oxidation reactions occurring in those regions. Additionally, as observed in Figure 20, O₂ mass fraction increases with elevation. At higher levels (11 m, 15 m, and 19 m), the distribution becomes more uniform across the width of the boiler. This uniformity is due to the minimal chemical activity occurring at these elevations, resulting in less O₂ consumption.

Figure 23 presents the variation of CO mass fraction along the vertical height of the boiler. Across all three measurement lines, the highest CO concentration appears near the base of the furnace and progressively decreases with elevation. As indicated in the figure, the CO mass fraction reaches approximately 0.13 along lines 1 and 3 near the coal inlet region, while a significantly lower value of about 0.01 is observed along line 2 in the central zone. The combustion of coal with 10% BFG produces more CO than coal alone due to BFG's 25% CO content, which reacts with O₂ to form CO₂. Minor reactions, including those with CO₂, H₂O, NO, and CH₄, also release CO but have a negligible impact compared to devolatilization and char oxidation. Figure 24 shows higher CO levels along the vertical plane near the coal inlet, while the front and back wall planes have lower CO. Figure 25 indicates intensified coal oxidation near the walls and char oxidation extending up to 500 mm above the distributor plate, with a peak rate of 0.023 k-mol/m³·s at line 3.

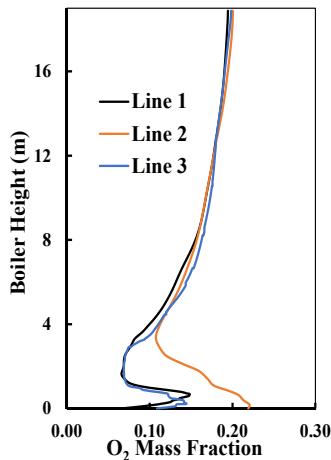


Figure 20. Oxygen concentration profile along boiler height

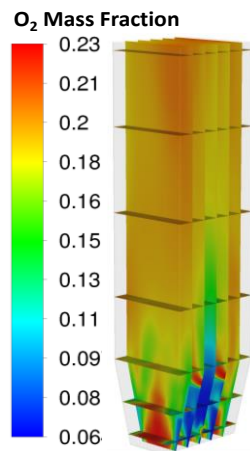


Figure 21. O₂ distribution contour

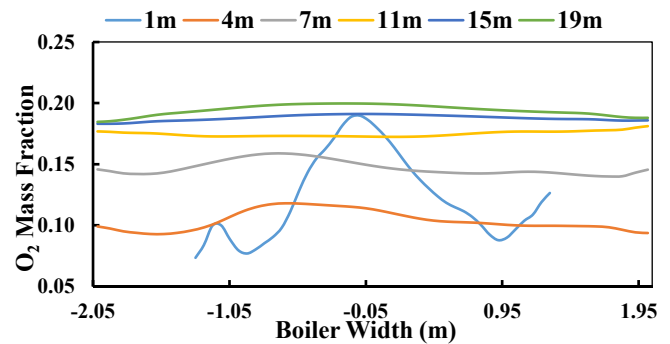


Figure 22. Lateral O₂ concentration

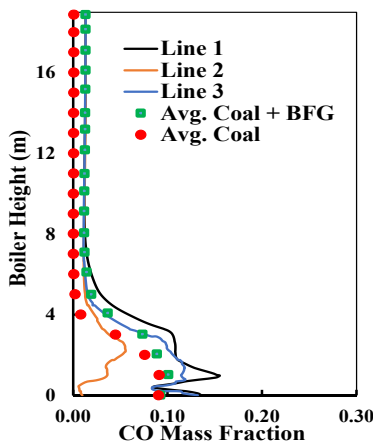


Figure 23. CO mass fraction variations

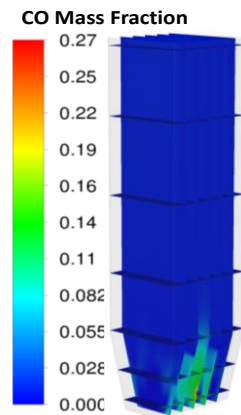


Figure 24. CO concentration

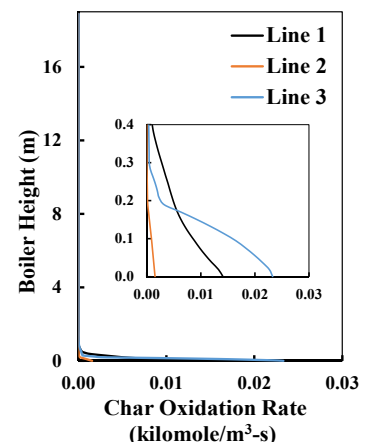


Figure 25. Coal char oxidation rate

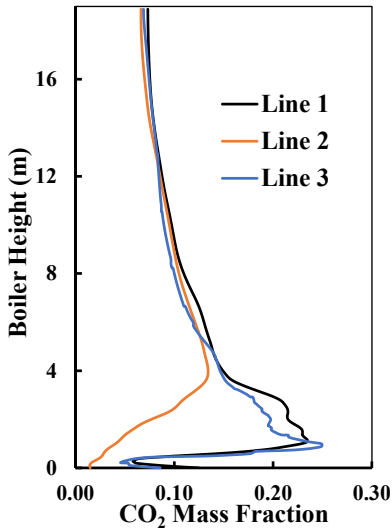


Figure 26. CO₂ concentration

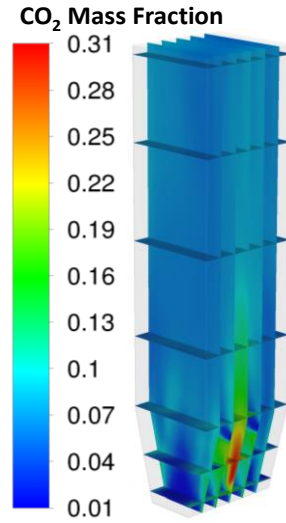


Figure 27. Predicted CO₂ concentration

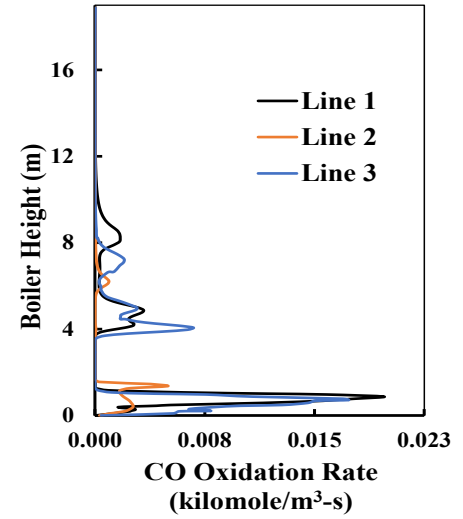


Figure 28. CO oxidation rate

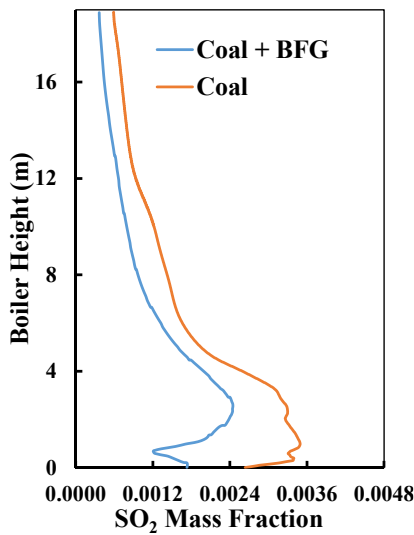


Figure 29. Variations of SO₂ mass fractions

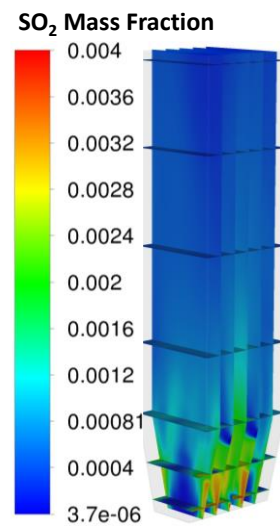


Figure 30. Predicted SO₂ concentration contours

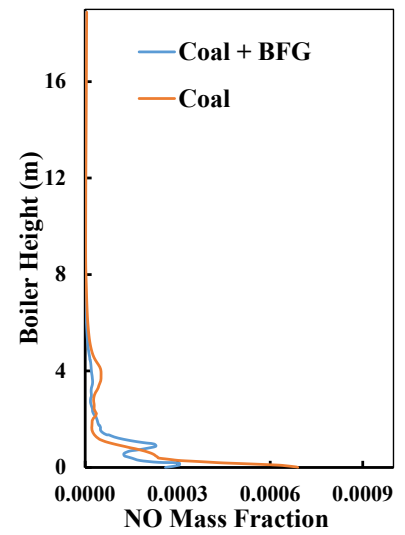


Figure 31. Variations of no mass fractions

Figure 26 presents the CO₂ mass fraction variation along three vertical lines in the boiler. CO₂ levels rise to 3.5 m due to the oxidation of CO in the lower fluidized bed region. Beyond 4 m, the CO₂ concentration gradually decreases, reaching its lowest point near the boiler outlet. Lines 1 and 3 show higher CO₂ concentrations at the bottom compared to line 2, as they are closer to the coal inlets, while line 2 is centrally located. CO oxidation, devolatilization, tar oxidation, and CO-NO reactions are the main processes that lead to the creation of CO₂, with CO oxidation and devolatilization being the main contributions.

Figure 27 displays CO₂ mass fraction contours on multiple horizontal and vertical cross-sections of the boiler. The maximum CO₂ concentration occurs in the lower central portion of the furnace and gradually decreases with increasing height. Lower CO₂ levels are observed near the front and rear walls relative to the core region. Figure 28 illustrates the CO oxidation rate along three vertical measurement lines. Along lines 1 and 3, the oxidation rate rises with height up to approximately 2 m above the distributor plate and reaches a peak value of about 0.021 k-mol/m³·s near 1.5 m. Above this point, the rate declines due to fuel injection at 2 m, where coal and 10% BFG react with O₂. Beyond 9 m, the oxidation rate

drops to zero, indicating no CO₂ formation in the upper region of the boiler.

4.2 Pollutant formation

Fossil fuel combustion releases harmful pollutants like SO₂, NO, and NO₂. In CFBC boilers, SO₂ is primarily generated from the reaction of sulphur in char with oxygen. Additional contributions come from char reacting with CO₂, H₂O, NO, and from H₂S oxidation. Figure 29 shows that SO₂ mass fractions are highest up to 3 m in the fluidized bed for both pure coal and coal with 10% BFG, due to intense char oxidation. Above this height, SO₂ levels decline and reach a minimum at the boiler outlet. The blended fuel produces less SO₂ than pure coal, as BFG contains no sulphur and dilutes the overall sulphur content. Figure 30 displays SO₂ mass fraction contours, showing higher concentrations in the bottom central region where coal oxidation is most active, and lower levels near the front and back walls. NO_x formation in CFBC boilers mainly originates from fuel-bound nitrogen, as thermal NO_x is negligible at typical operating temperatures (800–900 °C). NO forms through reactions between char and O₂, CO₂, and H₂O, while it is consumed by reactions involving NH₃ and

char. Figure 31 shows NO mass fractions peaking in the lower region and decreasing with height. Pure coal generates slightly more NO due to its higher nitrogen content. Figure 32 confirms these trends, showing low NO formation near the bottom and its gradual reduction in the freeboard due to consumption in downstream reactions, resulting in minimal NO levels at the boiler outlet. The predicted NO emissions are within the permissible limits prescribed by the Central Pollution Control Board (CPCB) for coal-fired boilers. However, further reduction strategies may be required to meet stricter norms for newer installations.

Figure 33 presents the evolution of the sand volume fraction

at different simulation times. At $t = 0$ s, the sand layer is fully settled on the distributor plate. Once the simulation begins and primary air is introduced, a portion of the particles becomes suspended, rising to roughly 2 m before falling back toward the base. Bubble formation is clearly visible in the lower section of the fluidized bed. The bed surface acts as a dynamic interface where bubbles grow, rise, and burst. These bubble motions generate strong mixing and turbulence throughout the bed, originating near the distributor and dissipating at the free surface. Such turbulence enhances gas–solid contact, leading to improved combustion efficiency and increased heat and mass transfer within the reactor.

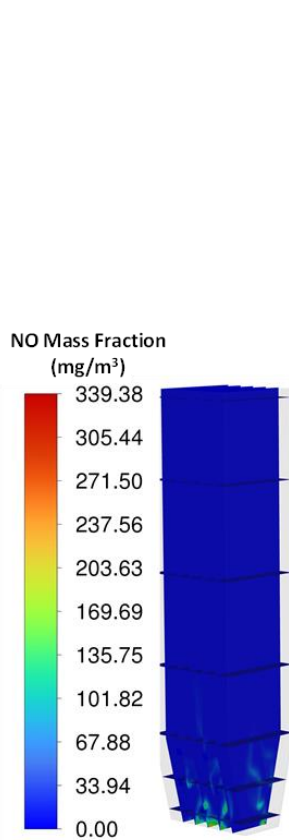


Figure 32. NO mass fraction contour for 10% BFG blends with coal

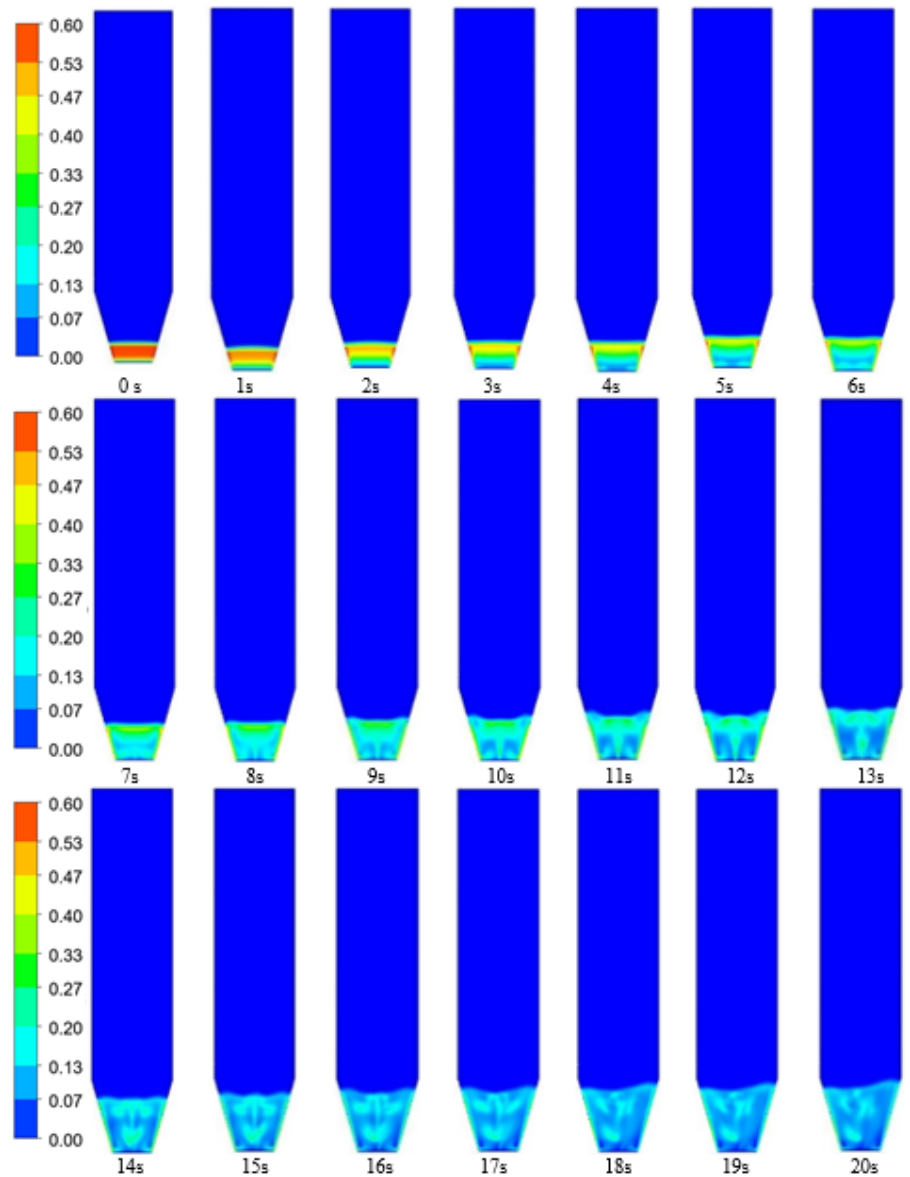


Figure 33. Sand Volume fraction at different time intervals

5. CONCLUSIONS

Three-dimensional CFD simulations are performed on an industrial-scale CFBC boiler operating in an integrated steel facility to investigate hydrodynamic behavior and combustion performance under two conditions: pure coal firing and co-firing with a blend of 10% BFG and 90% coal. The system is modeled as a multiphase flow consisting of four interacting

Eulerian phases — sand, coal, and the gas mixture — using an Eulerian–Eulerian framework coupled with the KTGF. Field measurements collected from plant operation, including temperature profiles, pressure distribution, bed height, suspension density, and void fraction, are employed to validate the numerical model. After validation, the same CFD approach is applied to evaluate boiler performance under blended fuel operation. The principal findings derived from the

hydrodynamic and combustion analysis of the coal–BFG mixture are summarized below.

- For both coal and blended fuels, a greater pressure drop is seen close to the fluidized bed's bottom and diminishes with height. When compared to pure coal, blended fuel exhibits a marginally smaller pressure drop (8%, 12% reduction), suggesting better fluid movement. In industrial processes, this decrease in pressure drop can improve fluidized bed efficiency and reduce energy usage.
- A relatively high sand volume fraction is observed under both pure coal firing and blended fuel operation. Increasing the concentration of bed material near the wall region can enhance heat transfer between the hot flue gases and the furnace walls. However, excessive accumulation of solids in this region may promote particle agglomeration. Therefore, maintaining an optimal sand concentration near the walls is important to ensure stable and trouble-free operation.
- The circulation pattern of solids and gas phases within the CFBC boiler promotes strong intermixing, with sand particles rising through the central core and descending along the near-wall region. This behavior, supported by axial velocity and vector field results, enhances internal recirculation. Such continuous solids circulation is critical for achieving uniform and efficient fuel combustion inside the reactor.
- When burning mixed fuels, the mass proportion of SO₂ and NO decreases. Decreasing SO₂ and NO emissions improves the air quality and supplements the CFBC boiler in achieving and fulfilling environmental rules and emission restrictions. Higher SO₂ emissions induce corrosion in the flue gas route and downstream components. Reduction in the SO₂ mass fraction by using BFG mixture fuel has the potential to increase the longevity of components and mitigate expenses associated with maintenance of the components.
- Using the Eulerian-Eulerian multiphase model, the simulation effectively creates a thorough CFBC coal combustion model by considering coal, sand, and gas in various stages. A comprehensive physics picture of a large-scale CFBC boiler is provided by mathematical modelling, which is also useful for modelling the combustion of coal and other biofuels.

REFERENCES

- [1] Ahmed, A.A., Trubaev, P.A., Ahmed, A.A., Trubaev, P.A., Nazzal, I.T. (2025). Combustion of granulated solid fuels and wood and domestic waste processing: A comprehensive review. *International Journal of Energy Production and Management*, 10(2): 207-221. <https://doi.org/10.18280/ijepm.100205>
- [2] Zhao, S., Wei, R. (2023). Mixed combustion characteristics of various biomass particles. *Journal of Sustainability for Energy*, 2(1): 19-28. <https://doi.org/10.56578/jse020102>
- [3] Cuervo-Piñera, V., Cifrián-Riesgo, D., Nguyen, P.D., Battaglia, V., et al. (2017). Blast furnace gas based combustion systems in steel reheating furnaces. *Energy Procedia*, 120: 357-364. <https://doi.org/10.1016/j.egypro.2017.07.215>
- [4] Tang, G., Silaen, A.K., Wu, B., Zhou, C.Q., et al. (2015). Numerical simulation of an industrial fluid catalytic cracking regenerator. *Journal of Thermal Science and Engineering Applications*, 7(2): 021012. <https://doi.org/10.1115/1.4029209>
- [5] Banerjee, S., Agarwal, R.K. (2015). Transient reacting flow simulation of spouted fluidized bed for coal-direct chemical looping combustion. *Journal of Thermal Science and Engineering Applications*, 7(2): 021016. <https://doi.org/10.1115/1.4029951>
- [6] Zhang, L., Xie, W., Ren, Z. (2020). Combustion stability analysis for non-standard low-calorific gases: Blast furnace gas and coke oven gas. *Fuel*, 278: 118216. <https://doi.org/10.1016/j.fuel.2020.118216>
- [7] Agarwal, G., Lattimer, B., Ekkad, S., Vandsburger, U. (2012). Experimental study on solid circulation in a multiple jet fluidized bed. *AIChE Journal*, 58(10): 3003-3015. <https://doi.org/10.1002/aic.13703>
- [8] Soares, G.C.P., Moreira, J.V.R., Santos, F.H.B., Guerra, D.R.S., Nogueira, M.F.M. (2024). Combustion process of coal–açai seed mixtures in a circulating fluidized bed boiler. *Energies*, 17(18): 4635. <https://doi.org/10.3390/en17184635>
- [9] Liu, H., Li, S., Xiang, X., Gong, S., Jia, C., Wang, Q., Sun, B. (2024). Simulation of biogas co-combustion in CFB boiler: Combustion analysis using the CPFD method. *Case Studies in Thermal Engineering*, 59: 104610. <https://doi.org/10.1016/j.csite.2024.104610>
- [10] Wang, Y., Chen, X., Xu, L., Ma, M., et al. (2024). Computational particle fluid dynamics simulation on combustion characteristics of blended fuels of coal, biomass, and oil sludge in a 130 t h⁻¹ circulating fluidized bed boiler. *Energies*, 17(1): 149. <https://doi.org/10.3390/en17010149>
- [11] Mahajan, V.V., Padding, J.T., Nijssen, T.M.J., Buist, K.A., Kuipers, J.A.M. (2018). Nonspherical particles in a pseudo-2D fluidized bed: Experimental study. *AIChE Journal*, 64(5): 1573-1590. <https://doi.org/10.1002/aic.16078>
- [12] Das, H.J., Mahanta, P., Saikia, R., Tamuly, P. (2021). Thermodynamic analysis in bubbling fluidized bed dryers with spiral and cone angles. *Journal of Thermal Science and Engineering Applications*, 13(6): 061019. <https://doi.org/10.1115/1.4050568>
- [13] Patankar, N.A., Joseph, D.D. (2001). Modeling and numerical simulation of particulate flows by the Eulerian–Lagrangian approach. *International Journal of Multiphase Flow*, 27(10): 1659-1684. [https://doi.org/10.1016/S0301-9322\(01\)00021-0](https://doi.org/10.1016/S0301-9322(01)00021-0)
- [14] Subramaniam, S. (2013). Lagrangian–Eulerian methods for multiphase flows. *Progress in Energy and Combustion Science*, 39(2-3): 215-245. <https://doi.org/10.1016/j.peccs.2012.10.003>
- [15] Van Buijtenen, M.S., Buist, K., Deen, N.G., Kuipers, J.A.M., Leadbeater, T., Parker, D.J. (2012). Numerical and experimental study on spout elevation in spout-fluidized beds. *AIChE Journal*, 58(8): 2524-2535. <https://doi.org/10.1002/aic.12765>
- [16] Ostermeier, P., DeYoung, S., Vandersickel, A., Gleis, S., Spliethoff, H. (2019). Comprehensive investigation and comparison of TFM, DenseDPM and CFD-DEM for dense fluidized beds. *Chemical Engineering Science*, 196: 291-309. <https://doi.org/10.1016/j.ces.2018.11.007>
- [17] Wu, Y., Liu, D., Hu, J., Ma, J., Chen, X. (2021). Comparative study of two fluid model and dense discrete phase model for simulations of gas–solid hydrodynamics

- in circulating fluidized beds. *Particuology*, 55: 108-117. <https://doi.org/10.1016/j.partic.2020.05.001>
- [18] Adnan, M., Sun, J., Ahmad, N., Wei, J.J. (2022). Validation and sensitivity analysis of an Eulerian-Eulerian two-fluid model (TFM) for 3D simulations of a tapered fluidized bed. *Powder Technology*, 396: 490-518. <https://doi.org/10.1016/j.powtec.2021.08.057>
- [19] Basu, D., Das, K., Smart, K., Ofoegbu, G. (2015). Comparison of Eulerian-Granular and discrete element models for simulation of proppant flows in fractured reservoirs. In *Proceedings of the ASME 2015 International Mechanical Engineering Congress and Exposition*. <https://doi.org/10.1115/IMECE2015-50050>
- [20] Ding, J., Gidaspow, D. (1990). A bubbling fluidization model using kinetic theory of granular flow. *AIChE Journal*, 36(4): 523-538. <https://doi.org/10.1002/aic.690360404>
- [21] Lun, C.K.K. (1991). Kinetic theory for granular flow of dense, slightly inelastic, slightly rough spheres. *Journal of Fluid Mechanics*, 233: 539-559. <https://doi.org/10.1017/S0022112091000599>
- [22] Emanuel, G. (1990). Bulk viscosity of a dilute polyatomic gas. *Physics of Fluids A*, 2: 2252-2254. <https://doi.org/10.1063/1.857813>
- [23] Gidaspow, D. (1994). *Multiphase Flow and Fluidization: Continuum and Kinetic Theory Descriptions*. Academic Press.
- [24] Mineto, A.T., Braun, M.P.D.S., Navarro, H.A., Cabezas-Gómez, L. (2014). Influence of the granular temperature in the numerical simulation of gas-solid flow in a bubbling fluidized bed. *Chemical Engineering Communications*, 201(8): 1003-1020. <https://doi.org/10.1080/00986445.2013.794138>
- [25] Neri, A., Gidaspow, D. (2000). Riser hydrodynamics: Simulation using kinetic theory. *AIChE Journal*, 46(1): 52-67. <https://doi.org/10.1002/aic.690460108>
- [26] Wen, C.Y., Yu, Y.H. (1966). A generalized method for predicting the minimum fluidization velocity. *AIChE Journal*, 12(3): 610-612. <https://doi.org/10.1002/aic.690120343>
- [27] Zhang, Y., Lei, F., Xiao, Y. (2015). Computational Fluid Dynamics simulation and parametric study of coal gasification in a circulating fluidized bed reactor. *Asia-Pacific Journal of Chemical Engineering*, 10(2): 307-317. <https://doi.org/10.1002/apj.1878>
- [28] Benzarti, S., Mhiri, H., Bournot, H., Occelli, R. (2014). Numerical simulation of turbulent fluidized bed with Geldart B particles. *Advanced Powder Technology*, 25(6): 1737-1747. <https://doi.org/10.1016/j.appt.2014.06.024>
- [29] Sahu, A.K., Raghavan, V., Prasad, B. (2019). Numerical simulation of gas-solid flows in fluidized bed gasification reactor. *Advanced Powder Technology*, 30(12): 3050-3066. <https://doi.org/10.1016/j.appt.2019.09.012>
- [30] Wu, Y., Liu, D., Ma, J., Chen, X. (2017). Three-Dimensional Eulerian-Eulerian simulation of coal combustion under air atmosphere in a circulating fluidized bed combustor. *Energy & Fuels*, 31(8): 7952-7966. <https://doi.org/10.1021/acs.energyfuels.7b01084>
- [31] Syamlal, M., Bissett, L.A. (1991). METC gasifier advanced simulation (MGAS) model. USDOE Morgantown Energy Technology Center, WV (United States). <https://www.osti.gov/biblio/10127635>.
- [32] Niksa, S., Liu, G., Hurt, R.H. (2003). Coal conversion submodels for design applications at elevated pressures. Part I. devolatilization and char oxidation. *Progress in Energy and Combustion Science*, 29(5): 425-477. [https://doi.org/10.1016/S0360-1285\(03\)00033-9](https://doi.org/10.1016/S0360-1285(03)00033-9)
- [33] Watanabe, H., Shimomura, K., Okazaki, K. (2013). Effect of high CO₂ concentration on char formation through mineral reaction during biomass pyrolysis. *Proceedings of the Combustion Institute*, 34(2): 2339-2345. <https://doi.org/10.1016/j.proci.2012.07.048>
- [34] Wang, X., Jin, B., Zhong, W. (2009). Three-dimensional simulation of fluidized bed coal gasification. *Chemical Engineering and Processing: Process Intensification*, 48(2): 695-705. <https://doi.org/10.1016/j.cep.2008.08.006>
- [35] Basu, P. (1999). Combustion of coal in circulating fluidized-bed boilers: A review. *Chemical Engineering Science*, 54(22): 5547-5557. [https://doi.org/10.1016/S0009-2509\(99\)00285-7](https://doi.org/10.1016/S0009-2509(99)00285-7)

NOMENCLATURE

| | |
|---------------------|---|
| k_{ash} | Ash Resistance |
| E | Activation Energy |
| \vec{g} | Acceleration due to Gravity |
| α_c | Coal Volume fraction |
| \dot{m}_c | Coal mass flow rate |
| v_c | Coal Velocity |
| ρ_c | Coal Density |
| θ_c | Coal granular temperature |
| P_c | Coal Pressure |
| d_c | Coal Particle diameter |
| μ_c | Coal Viscosity |
| T_c | Coal Temperature |
| γ_{θ_c} | Collisional Energy Dissipation |
| S_c | Coal source term due to mass transfer |
| D | Diffusivity |
| F_{ext} | External Force |
| k_{θ_c} | Diffusive constant |
| k | Dissipation of turbulent Kinetic Energy |
| k_{film} | Film Resistance |
| P | Gas Pressure |
| μ_g | Gas Viscosity |
| ρ_g | Gas Density |
| S_g | Gas source term due to mass transfer |
| T_g | Gas Temperature |
| v_g | Gas Velocity |
| \dot{m}_g | Gas mass flow rate |
| α_g | Gas Volume fraction |
| ρ_o | Initial density |
| Y_o | Initial Mass fraction of a chemical species |
| Y_p | Instantaneous Mass fraction of i^{th} species |
| Y | Instantaneous mass fraction of a chemical species |
| v_m | Mixture velocity |
| $\mu_{t,m}$ | Mixture turbulent viscosity |
| K_{gc} | Momentum exchange coefficient |
| $M_{w,i}$ | Molecular weight |
| $\alpha_{s,max}$ | Maximum Sawdust volume fraction |
| U_{mf} | Minimum fluidization velocity |
| ρ_m | Mixture Density |

| | | | |
|---------------------|--|---------------------|---|
| A | Pre-exponential Factor | $\overline{\tau}_c$ | Stress Tensor for Coal Phase |
| $g_{o,c}$ | Radial Particles Distribution function for coal | $\overline{\tau}_s$ | Stress Tensor for Sawdust Phase |
| $g_{o,s}$ | Radial Particles Distribution function for sawdust | S_s | Sawdust source term due to mass transfer |
| p | Partial Pressure | Sh | Sherwood Number |
| Re_c | Particles Reynolds number | ρ_s | Sawdust Density |
| $R_{i,r}$ | Reaction rate | I_{2D} | Second Invariant of Deviatorial Stress Tensor |
| v_{rc} | Relative Settling Velocity | μ_s | Sawdust Viscosity |
| e_{cc} | Restitution Coefficient coal particles | $G_{k,m}$ | Turbulent kinetic energy production |
| Y^* | Remaining mass fraction of a chemical species | R_{gas} | Universal Gas Constant |
| v_s | Sawdust Velocity | \hat{n} | Unit Normal Vector |
| θ_s | Sawdust granular temperature | \emptyset | Internal Frictional Angel |
| $\overline{\tau}_g$ | Stress Tensor for Gas Phase | | |
| \dot{m}_s | Sawdust mass flow rate | | |
| α_s | Sawdust Volume fraction | | |
| $v_{i,r}$ | Stoichiometric coefficient | | |
| T_s | Sawdust Temperature | | |
| P_s | Sawdust Pressure | | |
| K_{fr} | Rate of forward reaction | | |

Abbreviations

| | |
|------|---------------------------------|
| FBB | Fluidized bed Boiler |
| FBG | Fluidized bed Gasifier |
| FBR | Fluidized bed Riser |
| CFB | Circulating fluidized bed |
| KTGF | Kinetic theory of Granular flow |
| E-E | Eulerian-Eulerian |